A Method for Measuring the Complex Refractive Index of Low-Volume Materials Using Integrated Terahertz Time-Domain Transmissometry

Raphaël Pederiva, Philippe Artillan, Clément Geffroy, Christopher Bäuerle,
Jean-François Roux

HAL Id: hal-04722575
https://hal.univ-grenoble-alpes.fr/hal-04722575v1

Submitted on 5 Oct 2024

A method for measuring the complex refractive index of low-volume materials using integrated terahertz time-domain transmissometry

Raphaël Pederiva, Philippe Artillan, Clément Geffroy, Christopher Bäuerle, Jean-François Roux

Abstract—This study presents the development of an on-chip terahertz characterization process for low-volume or thin-film materials. A time-domain method based on the transmission of picosecond electrical pulses through the material to be characterized is proposed to determine the complex refractive index of materials up to hundreds of GHz. We demonstrate the capability of this method by determining the complex refractive index of a 15 nL droplet of glycerol over the 50-550 GHz frequency range.

Index Terms—THz, Refractive index, Glycerol, Photo Conductive Switch, On-Chip THz

I. INTRODUCTION

THE characterization of the refractive index of low-volume or thin-film materials in the microwave range can be performed by numerous methods, which always implies a compromise between the measurement accuracy and the attainable frequency range. Highest accuracy can be obtained at a single frequency using resonant cavities or resonators [1]. Wider bandwidth analysis can be achieved by sweeping the source frequency of an impedance analyzer or a vector network analyzer [2]. Single broadband measurements can be perfomed by time-domain methods, such as reflectometry or transmissometry, at the price of reduced accuracy [3].

In the THz range, optoelectronic generation of signals propagating in free space enables both frequency [4] and time domain [5] approaches. Due to the diffraction-limited size of the THz beam, characterizing small samples or thin films requires increasing the interaction length between the sample and the THz wave [6]. This can be done by using resonant electromagnetic structures such as metamaterials or waveguides placed in the THz beam [7], [8]. The resonant structure and the sample to be tested can also be integrated directly into the THz emitter; such an approach has made it possible to characterize micrometer-sized films [9] or very small quantities of liquid (sub-100 pL) [10]. However, for all of these techniques, the frequency range of interest is

limited by the spectral response of the resonant structure. On its side, the system introduced in the mid 1980's [11] which is based on the integration of photoconductive THz emitter and detector separated by a transmission line of a few mm long, is well adapted to broadband characterization of small samples or thin films. In fact, the transmission line, which can be covered by the sample to be characterized, is the test bed for this on-chip device, and its surface area, of the order of 0.1 mm², is well suited to samples with dimensions of less than a millimeter. This kind of device has been used to characterize solids [12], [13], but it is also well adapted to liquids as one can integrate a reservoir or a microfluidic channel above the THz circuit [14], [15]. This compact on-chip device can also be inserted into a cryostat, enabling, for example, the study of 2D materials physics at low temperatures [16], [17]. For spectroscopic applications, determining the dielectric constant of a material covering the transmission line requires modeling the propagation of THz pulses along the transmission line. Specially, for small low-losses samples, the question of possible multiple reflections inside the sample should be considered. Although a smart design of the on-chip system can prevent from such reflections [18], these latter can also support additional information and allow for simultaneous determination of dielectric and geometrical parameters, as demonstrated for the case of free-space propagation [19].

Our present work proposes a generalized characterization method, called THz Time-Domain Transmissometry (THz-TDT), for extracting the complex refractive index of any material under test (MUT) deposited onto an integrated measuring device. The proposed approach takes into account possible reflections at sample interfaces. Our approach is particularly relevant for small volumes of MUT such as a single droplet or a thin film. Our approach is intended to be applied to any integrated THz structure providing pulse generation and detection and the possibility to load and unload a MUT, such as a coplanar stripline [20], a parallel plate [21] or a microstrip line equipped with a reservoir [15]. We have developed this method for the case of an all integrated optoelectronic device which consists in a coplanar waveguide co-integrated with two ultrafast photoconductive switches (PCS) driven by a femtosecond laser. Finally, we applied this method to the characterization of a droplet of glycerol with a volume as low as 15 nL. This allow us to demonstrate and validate the proposed extraction method and to determine the complex refractive index of the liquid over a frequency band of more than 500 GHz.

Section II presents the experimental setup which consists of a time-domain measurement setup for measuring signals with and without a droplet of MUT. Secondly, the extraction scheme for obtaining the complex refractive index of the material under test (MUT) is described in Section III. The results allow for the extraction of glycerol complex refractive index in the 50-550 GHz range. Finally, the impact of the non-ideality of the PCS sampling is discussed and a validity domain for the method is proposed in Section IV.

II. EXPERIMENTAL SETUP

A. Test bench description

The MUT is characterized by a differential approach based on the processing of two time-domain signals provided by the measurement of the device in two configurations: unloaded (without MUT) and loaded (with MUT). The "differential transfer function" $H(\omega)$ is calculated as the ratio between the Fourier transform of the two signals by post-processing, as defined in eq. (3). This function then compares two different states of the device (unloaded/loaded) and is quite robust to measurement reproducible parasitics such as the effect of the access transmission lines. As we can see on fig. 1, the device is composed of a coplanar waveguide through which propagates a picosecond electrical pulse. THz pulses are generated and detected using fast Low-temperature-grown gallium arsenide (LTG-GaAs) photoconductive switches excited by two femtosecond laser beams. The time delay t_0 between the two pulses is controlled by an optical delay line with a fs resolution; a 10 fs time-step is typically used. Finally, the average value of the detection signal is measured for each t_0 with a lock-in amplifier (LIA) in order to increase the measurement sensitivity. We note that this on-chip integrated device can be fabricated on top of a GaAs wafer, but that a substrate such as quartz or a polymer material can be used thanks to the LTG-GaAs patch transfer technique (see for example [12]).
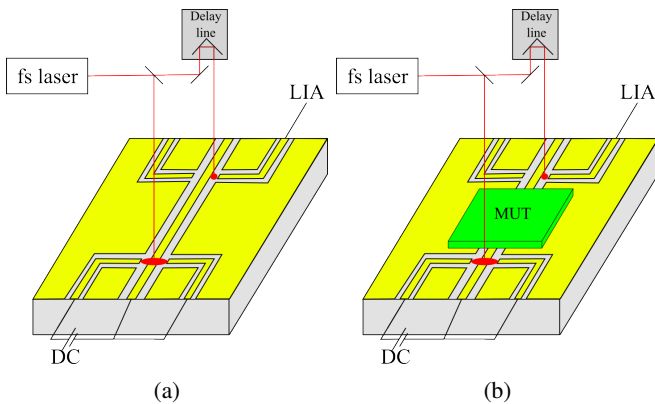

Fig. 1: Measurement setup for THz-TDT method. An electrical pulse is generated and detected by two PCS both excited by femtosecond laser pulses. (a) Unloaded device. (b) Device loaded with some material under test.

The complete device is fabricated on a 500 μm-thick Gallium Arsenide (GaAs) substrate, onto which a AlGaAs/ AlAs Bragg mirror (reflecting at 780 nm wavelength) and an upper 270 nm thick layer LTG-GaAs have been grown by Molecular Beam Epitaxy. The carrier trapping time of the LTG-GaAs layer is about 520 fs, as measured by time-domain optical reflectometry [22]. The RF circuit including the PCS structures is produced by photolithography of a 125 nm-thick layer of gold deposited on top of the LTG-GaAs layer. The central part of the structure is shown in fig. 2. It comprises the main CPW transmission line along which the THz pulses will propagate, and four lateral CPW lines that allows for the biasing of the generation PCS and the connection of the detection PCS to the LIA. The lateral dimensions of the main CPW waveguide are 30 μm for the central line and 20 μm for the gap in between this line and the ground planes, while the dimensions of the four lateral CPW lines are of 18 μm and 12 μm for the widths of the central electrode and the gap respectively. Four identical PCS are designed at the junctions in between the central and the 4 lateral CPW lines. The geometry of the PCS, which sensitivity is increased by means of interdigitated fingers (with a dimension of 2x15 μm), is detailed in the inset of fig. 2. The PCS are positioned by pairs, on each side of the main CPW central line in a manner that ensured a perfect axial symmetry of the device. The distance in between the two pairs of PCS is 980 μm. The axial symmetry of the arrangement is used in order to facilitate a better excitation of the quasi TEM mode of the CPW by symmetrical illumination and electrical biasing of the structure [23].
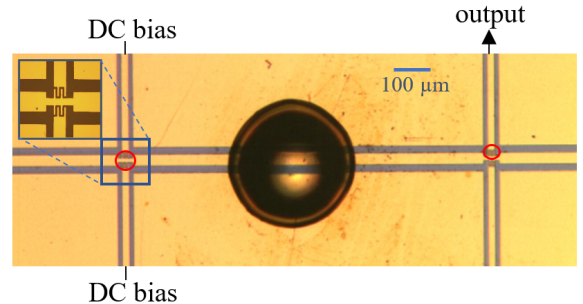

Fig. 2: THz-TDT device comprising two pairs of PCS. A droplet of glycerol was deposited on the device (approx. 15 nL) in between the generation and detection areas. Red circles show the positions of the laser spots for generation and detection pulses. The upper-left inset shows a detailed picture of the PCS.

In order to generate a short electrical pulse, both PCS on the left side of the device are symmetrically DC biased at 4 V by mean of a Keithley 2400 Source Meter Unit (SMU). This pair of PCS is then illuminated by a laser beam focused in the centre of the structure (left red circle in fig. 2) thanks to a lens with 50 mm focal length. On the right side of the device, a similar lens is used to excite one PCS that is used for the detection of the THz pulse propagating along the central CPW waveguide. When this PCS is illuminated, a part of the signal is sampled and measured by a lock-in amplifier (SR530 from Stanford Research Systems) electrically connected to the output port (see fig. 2). Both the generation and detection

structures are illuminated by a train of 70 femtosecond optical pulses generated at 780 nm by a fiber laser (Menlo C fiber 780). The average optical power used is around 5 mW per beam at a repetition rate of 100 MHz.
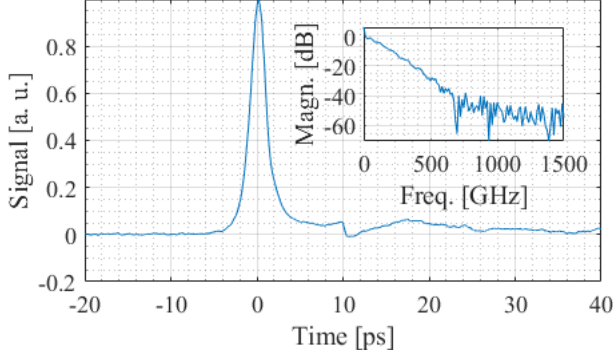
B. Device characterization

Fig. 3: Measured time-domain signal for the device and the magnitude of his spectrum in top right inset.

A typical signal generated and detected using the unloaded device is shown in fig. 3. The main electrical peak has a full width at half maximum of 2 ps. This short duration leads to a broadband spectrum presented in the inset of fig. 3. It was recorded with a single scan of the optical delay line and a lock-in amplifier with a time constant of 100 ms. The observed dynamic is 40 dB and the noise floor is reached around 600 GHz, thus establishing the upper frequency limit of the test bench. Replica of this main pulse may be observed because of possible reflections at any discontinuity of the RF circuit. In the present case, the first of these replica is measured for a time delay of 50 ps (not shown if fig. 3). However, a small parasitical reflection is detected at 10 ps, which is probably due to the weak excitation of a non CPW mode [24]. As a consequence of these spurious reflections, we will, for material characterization purposes, focus on the main peak and only consider a reduced time window.

III. APPLICATION TO MATERIAL CHARACTERIZATION

A. Transmission of a droplet of glycerol

To demonstrate the capabilities of our approach we intend to characterize the complex refractive index of a droplet of glycerol. To do so, a small volume of the liquid is deposited in between generation and detection areas as shown in fig. 2. The shape of the droplet is close to a dome, which diameter varies between 300 µm and 700 µm and height between 50 µm to 100 µm depending on the deposited volume. We note that thanks to physical properties of the glycerol, the droplet do not evaporate during the time of the experiment.

The incident electrical pulse propagating trough the unloaded and loaded CPW are measured in the same experimental conditions, i.e. with no modification of the optical alignment. The two measured output signals $v_{air}(t_0)$ (unloaded device) and $v_{mut}(t_0)$ (loaded device) are plotted in fig. 4.
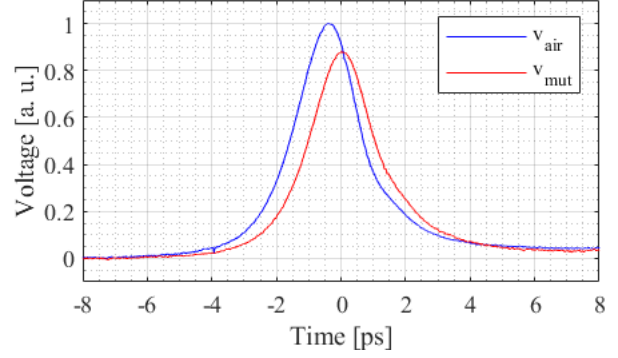

Fig. 4: Measured time-domain signals for the device unloaded (blue curve) and loaded with a glycerol droplet (red curve)
.

The droplet of glycerol is responsible for a significant delay (about 400 fs) and an amplitude attenuation (about 12 %) of the propagated pulse. We note that the observed delay is much larger than the jitter of our acquisition setup (9 fs). The latter is estimated empirically by repeating the same measurement tens of times and computing the drift of the pulse rising edge.

As explained above, both signals have been time-windowed with a Hann window of 15 ps width centered on each peak in order to eliminate spurious reflections. Fourier transforms of the two signals are then computed, and plotted in fig. 5. We have also calculated the ratio of the spectrum magnitudes and the difference of the spectrum phase that will be use in the extraction procedure.
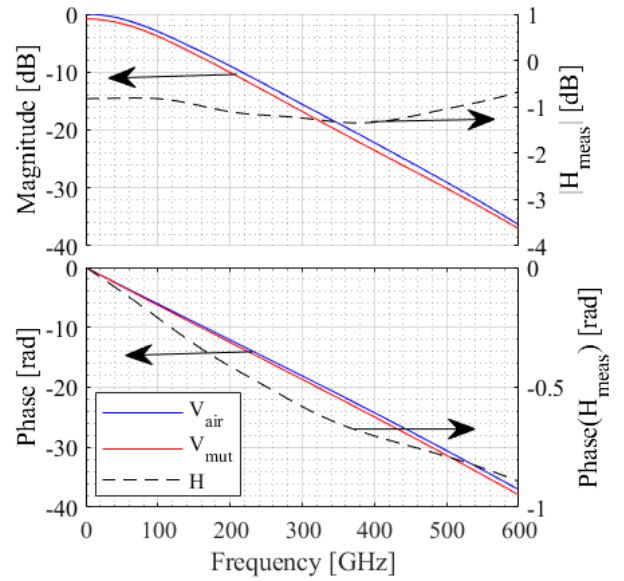

Fig. 5: Frequency-domain spectra corresponding to time-domain signals of fig. 4 represented in magnitude and phase. The dashed lines represent the complex ratio H_{meas} of the two spectra in magnitude and phase.

B. Theoretical expression of the frequency-domain transfer function

This part intends to define the differential transfer function $H(\omega)$ of the device and to demonstrate its theoretical expression. Fig. 6 presents the flow graphs of the propagation path of the pulse signal through the unloaded device (6.a) and through the loaded device (6.b). In the following development, the studied signals are frequency domain progressive voltage waves and regressive voltage waves. They are noted $V_i^+(\omega)$ and $V_i^-(\omega)$, where i is the name of the electrical node. They are defined as a combination of observable voltage $V_i(\omega)$, current $I_i(\omega)$ and the characteristic impedance of the transmission line $Z_i(\omega)$ through which the wave is propagating:

$$\begin{cases} V_i^+(\omega) = \frac{V_i(\omega)+Z_i(\omega)I_i(\omega)}{2} \\ V_i^-(\omega) = \frac{V_i(\omega)-Z_i(\omega)I_i(\omega)}{2}. \end{cases} \quad (1)$$

The input signal $V_{gen}^+(\omega)$ on the left of both flow graphs is a fast picosecond pulse. The two signals of interest are $V_{a_{air}}^+(\omega)$ and $V_{a_{mut}}^+(\omega)$ detected at the detection PCS. They respectively correspond to the pulses who had propagated through the transmission line unloaded or loaded with the MUT.
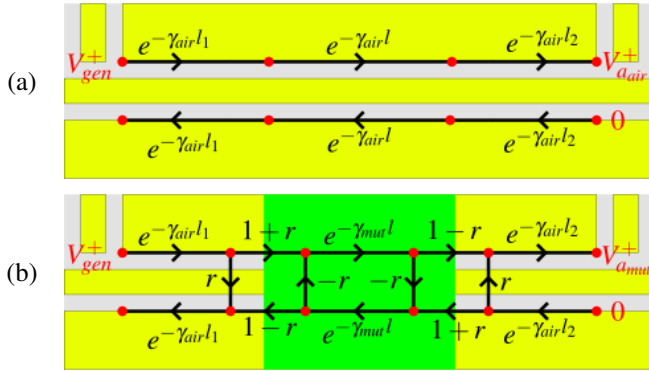

Fig. 6: Equivalent flow graph of the propagating path of the pulse. (a) Unloaded device. (b) Loaded device.

Furthermore, in fig. 6, γ_{air} is the propagation constant of the unloaded line, γ_{mut} is the propagation constant of the loaded line, l_1 and l_2 are the lengths of the access lines and l is the length of the unloaded/loaded line. Finally, $r(\omega)$ is the reflection coefficient at the AIR/MUT interface, defined as:

$$r(\omega) = \frac{Z_{mut}(\omega) - Z_{air}(\omega)}{Z_{mut}(\omega) + Z_{air}(\omega)}. \quad (2)$$

The function $H(\omega)$ defined as the ratio of the output signals $V_{a_{mut}}^+(\omega)$ and $V_{a_{air}}^+(\omega)$, can be expressed as:

$$H(\omega) = \frac{V_{a_{mut}}^+(\omega)}{V_{a_{air}}^+(\omega)} = \frac{1-r^2}{1-r^2 e^{-2\gamma_{mut}l}} e^{-(\gamma_{mut}-\gamma_{air})l}. \quad (3)$$

It is worth mentioning that all reflections inside the MUT are taken into account in eq. (3). Neglecting those reflections leads to a simpler expression of $H(\omega) = e^{-(\gamma_{mut}-\gamma_{air})l}$, as presented in [14], [18].

C. Generation of $H(\omega)$ lookup table by FEM simulation

As presented is eq. (2) and (3), $H(\omega)$ depends on Z_{air}, γ_{air}, Z_{mut} and γ_{mut}. In the case of freespace Terahertz time-domain Spectroscopy (THz-TDS), there exists a closed form expression for the electromagnetic (EM) field map, and $Z_{air} = Z_0$, $\gamma_{air} = \gamma_0$, $Z_{mut} = Z_0/n_{mut}$ and $\gamma_{mut} = n_{mut}\gamma_0$ (with $Z_0 = \sqrt{\mu_0/\varepsilon_0}$ the characteristic impedance of vacuum and $\gamma_0 = j\omega\sqrt{\mu_0\varepsilon_0}$ the propagation constant of vacuum) [25], [26], [27]. On the contrary, when the signal propagates on an integrated transmission line, these physical quantities cannot be directly determined in an analytical way and the common approach is to use physical simulation. Z_{air}, γ_{air}, Z_{mut} and γ_{mut} are computed by Finite Element Method (FEM) simulation, taking the geometry of the CPW transmission lines and the complex dielectric properties of the materials into account.

$$(Z_{air}, \gamma_{air}) \xleftarrow{FEM\ simulation} n_{air}, \quad (4)$$

$$(Z_{mut}, \gamma_{mut}) \xleftarrow{FEM\ simulation} n_{mut}. \quad (5)$$

The FEM simulations performed at steps (4) and (5) are aimed at computing $Z = \sqrt{\frac{R+jL\omega}{G+jC\omega}}$ and $\gamma = \sqrt{(R+jL\omega)(G+jC\omega)}$, where R, L, G and C are the primary parameters of the simulated transmission lines [28]. 2D simulations are conducted for computing time efficiency since the transmission line segment is considered translation invariant along the propagation direction while the MUT is modeled as a rectangular box with lateral dimensions much larger than the CPW structure. R and L are computed with a 2D quasistatic magnetic solver (Ansys Electronics Desktop Q2D magnetic solver), to take into account the impact of the conductivity of the conductors and the substrate. The computation of G and C is then performed with a 2D quasistatic electrical solver (Ansys Electronics Desktop Q2D electrical solver) to take into account the impact of the complex permittivity of the dielectric materials (air, substrate, MUT). Especially, the computation of step (4) is performed only once to compute Z_{air} and γ_{air} knowing n_{air} and l. The computation of step (5) is performed for a large 2D set of realistic complex n_{mut} (typically 2000 points, the real part ranging from 1 to 4 and the imaginary part from 0 to 1) to obtain a set of Z_{mut} and γ_{mut}. A 2D look-up table $H_{lookup}(n_{mut})$ is then numerically computed using (2) and (3). This procedure is independently repeated for each frequency point.

D. Refractive index determination from the lookup table

The look-up table $H_{lookup}(n_{mut})$, computed in previous section, is bijective for the studied range of n_{mut}. H_{lookup} can then be inverted and interpolated in a numerical function H_{lookup}^{-1} that provides n_{mut} as a function of H as illustrated in fig. 7 for the real part of the refractive index (given for one frequency value).

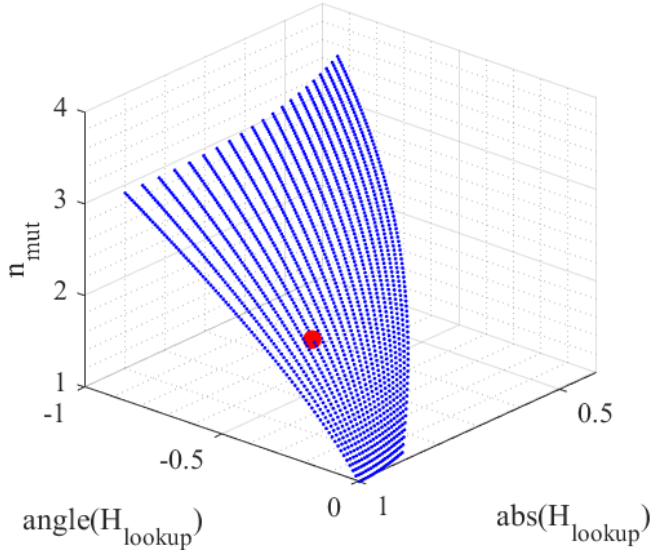$$n_{mut} = H_{lookup}^{-1}(H). \quad (6)$$

Fig. 7: Inverted look-up table H^{-1}_{lookup} (blue points) at 150 GHz, and the refractive index (red point) extracted form measured H_{meas}.

Fig. 8: Experimental extracted values of the refractive index n of 8 droplets of glycerol at room temperature (296.5°K): real part part n' (a) and imaginary part κ (b). Our method (blue line) is compared to [30] obtained by THz-TDS at room temperature, and to [29] obtained by fitting a empirical model to experimental data measured at 295°K on various frequency ranges.

In order to determine the refractive index, the numerical function H^{-1}_{lookup} is applied to the experimental transfer function $H_{meas} = V_{mut}(\omega)/V_{air}(\omega)$. This latter is calculated as the ratio of the two Fourier transforms of the experimental signals, plotted in dashed lines in fig. 5.a and 5.b. As observed in fig. 7, magnitude and phase of H_{meas} give the refractive index of the MUT (red point). This procedure is repeated independently for all frequencies. It is important to mention that the two actually measured signals $v_{air}(t_0)$ and $v_{mut}(t_0)$ are equivalent-time signals measured through the detection PCS and the LIA. Hence, their Fourier transforms are not equal to $V^+_{a_{air}}(\omega)$ and $V^+_{a_{mut}}(\omega)$ used to define H in eq. (3). The ratio $V^+_{a_{mut}}(\omega)/V^+_{a_{air}}(\omega)$ and the ratio $V^+_{mut}(\omega)/V^+_{air}(\omega)$ can however be considered equal under some assumptions that will be discuss in section IV.

We have applied this procedure to the study of some glycerol droplets that have been presented in section III-A. This has been done for eight different volumes of liquid ranging from 10 to 200 nL. The extracted value of the complex refractive index in the 50-550 GHz frequency range is shown in fig. 8 for each measurement. Experimental values from literature [29], [30], [31] for pure glycerol at room temperature have also been reported. Both the real part n' (decreasing from 2.1 to 1.8 in frequency) and the losses κ (decreasing from 0.5 to 0.1) are in good agreement with literature.

E. Considerations on uncertainties

Eight measurements have then been done with different droplet sizes in order to evaluate the variability (or random sources of uncertainty). Fig. 8 presents the results of the extracted values. The experiments are quite reproducible and the difference between extracted curves can mainly be explain by the error on the determination of the length of the MUT.
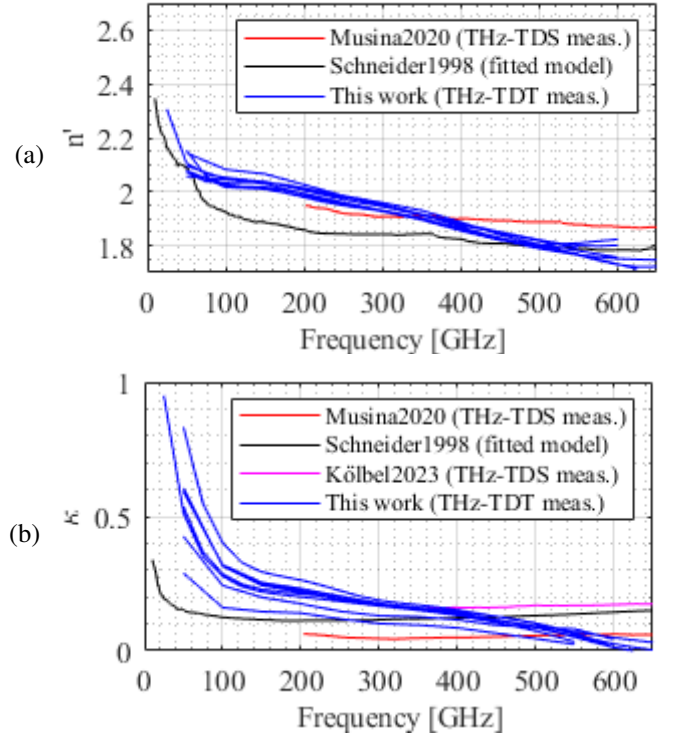
This latter dimension is estimated by optical microscopy before the extraction procedure.

Moreover, this kind of experiment may suffer from systematic experimental sources of uncertainties, such as beam optical alignment, long term laser instability, etc. The extraction scheme based on FEM simulation of the transmission line cross-section also introduces systematic error due to the uncertainties on physical properties of the materials (conductivity of the conductors, complex refractive index of the substrate) and on the geometrical dimensions of the device.

The differential approach (unloaded/loaded) is intended to reduce the impact of those systematic errors.

IV. IMPACT OF EQUIVALENT TIME SAMPLING

The input of the extraction scheme presented in part III is $H(\omega)$ defined, in eq. (3), as the ratio of the real time propagating signals $v^+_{a_{air}}(t)$ and $v^+_{a_{mut}}(t)$. These signals are too fast to be directly measured and the experimental setup only gives access to the equivalent time signals $\tilde{v}^+_{b_{air}}(t_0)$ and $\tilde{v}^+_{b_{mut}}(t_0)$ (called $v_{air}(t_0)$ and $v_{mut}(t_0)$ is section III). In order to highlight the differences between the real time signal $v^+_{a_{air}}(t)$ and the equivalent time signal $\tilde{v}^+_{b_{air}}(t_0)$, they have both been simulated by using a circuit solver (Keysight ADS) coupled with numerical computation. Fig. 9 shows those

simulated signals. The equivalent time signal shows a much longer rise time than the real time signal due to the picosecond response time of the sampler. As a consequence one cannot consider that these two signals are similar contrary to the case were PCS are used to sample gigahertz frequency signals [32], [33]. However, this section provides a full study of the validity of the approximation of using equivalent time signals to define $H(\omega)$ and the associated assumptions.
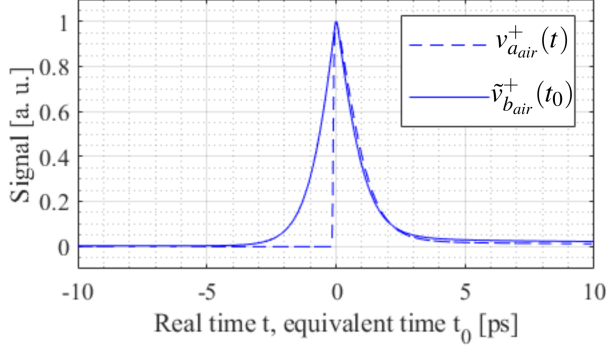

Fig. 9: Simulated real time signal (unmeasurable signal) versus equivalent time sampled signal (measured signal).

A. General relationship between real time and equivalent time signals

Fig. 10 shows the equivalent electrical circuit of the detection arm involving the detection PCS and the LIA.
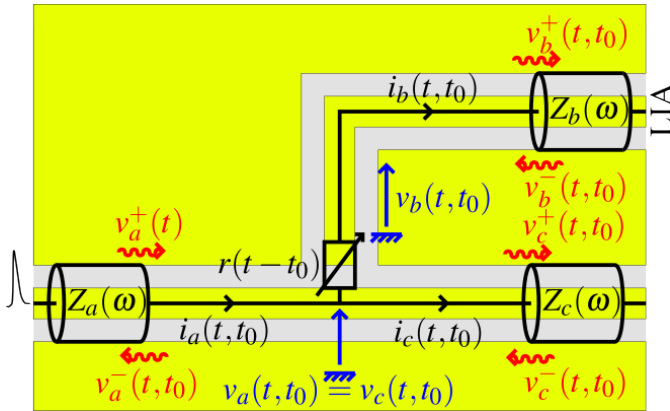

Fig. 10: Equivalent circuit model of the detection area.

The incident progressive voltage wave $v_a^+(t)$ is the pulse which propagated through the unloaded or loaded CPW transmission line. The incident pulse is sampled by the detection PCS, modeled by a time varying resistor $r(t-t_0)$, t_0 being the instant when the femtosecond laser excites the PCS (capacitive effects are neglected). The detection is then performed by a lock-in amplifier that receives the progressive voltage wave $v_b^+(t, t_0)$. Finally, the LIA provides the average value $\tilde{v}_b^+(t_0)$ of $v_b^+(t, t_0)$ for each equivalent time t_0 (corresponding to a position of the delay line):

$$\tilde{v}_b^+(t_0) \propto \int_{t=0}^{T} v_b^+(t, t_0)\, dt. \tag{7}$$

In addition to eq. (1), the relationship between the incident voltage wave $v_a^+(t, t_0)$ and the sampled voltage wave $v_b^+(t, t_0)$ can be established from fig. 10 by writing the system of equations of the equivalent circuit:

$$\begin{cases} v_a(t) + z_a(t) * \left(\frac{v_a(t) - v_b^+(t, t_0)}{r(t - t_0)} + i_c(t, t_0) \right) = 2v_a^+(t) \\ v_b^+(t, t_0) = z_b(t) * i_b(t, t_0) \\ v_a(t) = z_c(t) * i_c(t, t_0) \\ r(t - t_0)i_b(t, t_0) + v_b^+(t, t_0) = v_a(t), \end{cases}$$
$$(8)$$

where $z_i(t) = \mathfrak{F}^{-1}[Z_i(\omega)]$ is the inverse Fourier transform of the frequency dependent characteristic impedance of transmission line i. The only assumption here is that there is no reflected signals $v_b^-(t, t_0)$ or $v_c^-(t, t_0)$. This assumption is valid within a limited time window, and depends on the length of the access transmission lines.

With no further assumption, it is impossible to invert the global system of equations (7-8) and the measured signal $\tilde{v}_b^+(t_0)$ cannot be expressed as a function of the incident real time voltage wave $v_a^+(t)$. However, this can be achieved in the special case of lossless transmission line.

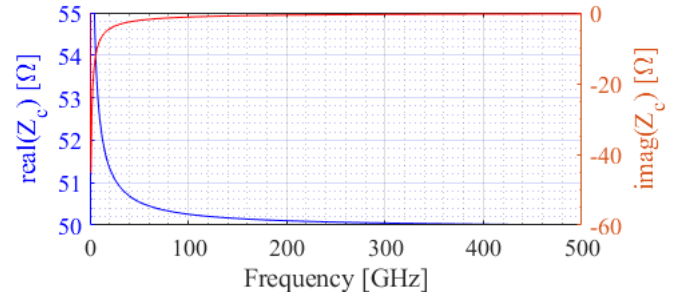### B. Special case of lossless transmission lines

Fig. 11: Simulated characteristic impedance for used CPW line. Above 50 GHz, the real part of the characteristic impedance varies of less than 1 % and the imaginary tends towards zero.

The simulated real and imaginary parts of the characteristic impedance $Z_c(\omega)$ of the CPW transmission line that we are using (20-30-20 μm geometry on GaAs substrate) are plotted in fig. 11. Beyond 50 GHz, the characteristic impedance can be considered real and constant in frequency. Similarly, the same behavior can be observed for $Z_a(\omega)$ and $Z_b(\omega)$ (not represented here). This, in particular, corresponds to the common case of almost lossless transmission lines ($Z_i = \sqrt{(R + jL\omega)/(G + jC\omega)}$), with L and C constant in frequency and $R = G = 0$).

Under the approximation of real and constant characteristic impedances Z_i, $z_i(t) = Z_i\delta(t)$ convolution products in the system of equations (8) can be replaced by multiplications by Z_i. Furthermore, Z_i being real ensures all signals to be real. The simplification of the system of equations (8) leads to a relationship between $v_b^+(t, t_0)$ and $v_a^+(t)$:

$$v_b^+(t, t_0) = \underbrace{\frac{2 \; Z_b}{Z_a + Z_b + \frac{Z_a Z_b}{Z_c} + \; r\,(t - t_0)\left(1 + \frac{Z_a}{Z_c}\right)}}_{m(t-t_0)} \; v_a^+(t). \tag{9}$$

The definition of a function $m(t-t_0)$ is given in eq. (9). This function captures the sampling effect of the PCS. Injecting eq. (9) in eq. (7), leads to a closed form expression of the equivalent time signal being measured $\tilde{v}_b^+(t_0)$:

$$\tilde{v}_b^+(t_0) \propto \; m(-t_0) * v_a^+(t_0). \tag{10}$$

The expression of the Fourier transform of $\tilde{v}_b^+(t_0)$ then becomes:

$$\tilde{V}_b^+(\omega) \propto \mathfrak{F}[m(-t_0)] \; V_a^+(\omega) \; . \tag{11}$$

And finally, applying eq. (11) to both the measured signals $\tilde{V}_{b_{air}}^+(\omega)$ and $\tilde{V}_{b_{mut}}^+(\omega)$ allows to demonstrate that the ratio $H(\omega)$ used for the extraction of the complex refractive index defined in eq. (3) can also be computed as:

$$H(\omega) = \frac{V_{a_{mut}}^+(\omega)}{V_{a_{air}}^+(\omega)} \approx \frac{\tilde{V}_{b_{mut}}^+(\omega)}{\tilde{V}_{b_{air}}^+(\omega)}. \tag{12}$$

As a consequence, the impact of the equivalent time sampling is then negligible for refractive index extraction if all transmission lines are almost lossless, which occurs in practice at high enough frequency.

V. CONCLUSION

The feasibility of extracting the complex refractive index of a droplet of material by a time-resolved optoelectronic transmissometry method has been demonstrated from 50 to 550 GHz. Validation is performed on a small volume droplet (15 nL) of glycerol by comparison with data from literature. Finally, this approach opens the way towards the creation of a laboratory on chip for the analysis in the 50-550 GHz range of low volumes of materials such as films, droplets or microfluidics channels.

ACKNOWLEDGMENT

REFERENCES

[1] J. Krupka, "Frequency domain complex permittivity measurements at microwave frequencies," *Measurement Science and Technology*, vol. 17, no. 6, p. R55, Apr. 2006.

[2] J. P. Dunsmore, *Handbook of Microwave Component Measurements: with Advanced VNA Techniques*. Wiley, 2012.

[3] E. Pettinelli *et al.*, "Time domain reflectometry: Calibration techniques for accurate measurement of the dielectric properties of various materials," *Review of Scientific Instruments*, vol. 73, no. 10, pp. 3553–3562, Oct. 2002.

[4] D.-Y. Kong *et al.*, "High resolution continuous wave terahertz spectroscopy on solid-state samples with coherent detection," *Optics Express*, vol. 26, no. 14, pp. 17 964–17 976, Jul. 2018.

[5] J.-L. Coutaz *et al.*, *Principles of Terahertz Time-Domain Spectroscopys*. Jenny Stanford Publishing, 2018.

[6] J. F. O'Hara *et al.*, "A Review on Thin-film Sensing with Terahertz Waves," *Journal of Infrared, Millimeter, and Terahertz Waves*, vol. 33, no. 3, pp. 245–291, Mar. 2012. [Online]. Available: https://doi.org/10.1007/s10762-012-9878-x

[7] Y. Laamiri *et al.*, "Thin-film characterization by terahertz time-domain spectroscopy using grating-assisted excitation of guided modes," *Applied Physics Letters*, vol. 94, no. 7, p. 071106, 02 2009.

[8] R. Zhang *et al.*, "Terahertz microfluidic metamaterial biosensor for sensitive detection of small-volume liquid samples," *IEEE Transactions on Terahertz Science and Technology*, vol. 9, no. 2, pp. 209–214, 2019.

[9] W. Withayachumnankul *et al.*, "Sub-diffraction thin-film sensing with planar terahertz metamaterials," *Opt. Express*, vol. 20, no. 3, pp. 3345–3352, Jan 2012.

[10] K. Serita *et al.*, "I-design terahertz microfluidic chip for attomole-level sensing," *Journal of Physics: Photonics*, vol. 4, no. 3, p. 034005, 2022.

[11] D. H. Auston, *Picosecond Optoelectronic Devices*. edited by Chi H. Lee (Academic, London), 1984, ch. 4, pp. 73–117.

[12] C. Wood *et al.*, "On-chip pulsed terahertz systems and their applications," *International Journal of Infrared and Millimeter Waves*, vol. 27, no. 4, pp. 557–569, Apr. 2006.

[13] M. B. Byrne *et al.*, "Terahertz vibrational absorption spectroscopy using microstrip-line waveguides," *Applied Physics Letters*, vol. 93, no. 18, p. 182904, Nov. 2008.

[14] M. Swithenbank *et al.*, "On-chip terahertz-frequency measurements of liquids," *Analytical Chemistry*, vol. 89, no. 15, pp. 7981–7987, Aug. 2017.

[15] S. Kasai *et al.*, "Micro Strip Line-Based On-Chip Terahertz Integrated Devices for High Sensitivity Biosensors," *Applied Physics Express*, vol. 2, no. 6, p. 062401, May 2009.

[16] P. Gallagher *et al.*, "Quantum-critical conductivity of the dirac fluid in graphene," *Science*, vol. 364, no. 6436, pp. 158–162, 2019.

[17] J. Wu *et al.*, "Excitation, detection and electrostatic manipulation of terahertz-frequency range plasmons in a two-dimensional electron system," *Scientific Reports*, vol. 5, no. 1, p. 15420, 2015.

[18] M. Swithenbank, "Terahertz Spectroscopy in Microfluidic Systems," phd, University of Leeds, Aug. 2017. [Online]. Available: https://etheses.whiterose.ac.uk/18515/

[19] L. Duvillaret *et al.*, "Highly precise determination of optical constants and sample thickness in terahertz time-domain spectroscopy," *Appl. Opt.*, vol. 38, no. 2, pp. 409–415, Jan 1999.

[20] J. Lee *et al.*, "On-chip terahertz sensor based on low-loss coplanar strip lines for the analysis of microscale two-dimensional materials," *2022 47th International Conference on Infrared, Millimeter and Terahertz Waves (IRMMW-THz)*, pp. 1–2, 2022.

[21] N. Laman *et al.*, "High-resolution waveguide thz spectroscopy of biological molecules," *Biophysical journal*, vol. 94, no. 3, pp. 1010–1020, Apr. 2008.

[22] J.-F. Roux *et al.*, "Time-resolved reflectivity characterization of polycrystalline low-temperature-grown gaas," *Applied Physics Letters*, vol. 74, no. 17, pp. 2462–2464, Apr. 1999.

[23] N. Zamdmer *et al.*, "Mode-discriminating photoconductor and coplanar waveguide circuit for picosecond sampling," *Applied Physics Letters*, vol. 74, no. 7, pp. 1039–1041, Feb. 1999.

[24] J. Allam *et al.*, "Monolithically-integrated optoelectronic circuit for ultrafast sampling of a dual-gate field-effect transistor," *Optical and Quantum Electronics*, vol. 28, no. 7, pp. 875–896, Jul. 1996.

[25] L. Duvillaret *et al.*, "A reliable method for extraction of material parameters in terahertz time-domain spectroscopy," *IEEE Journal of Selected Topics in Quantum Electronics*, vol. 2, no. 3, pp. 739–746, Sept. 1996.

[26] H. Němec *et al.*, "Independent determination of the complex refractive index and wave impedance by time-domain terahertz spectroscopy," *Optics Communications*, vol. 260, no. 1, pp. 175–183, Apr. 2006.

[27] F. R. Faridi and S. Preu, "Pulsed free space two-port photonic vector network analyzer with up to 2 thz bandwidth," *Opt. Express*, vol. 29, no. 8, pp. 12 278–12 291, Apr 2021.

[28] D. M. Pozar, *Microwave engineering*. Wiley, 2012.

[29] U. Schneider *et al.*, "Dielectric and far-infrared spectroscopy of glycerol," *Journal of Non-Crystalline Solids*, vol. 235-237, pp. 173–179, Aug. 1998.

[30] G. R. Musina *et al.*, "Optimal hyperosmotic agents for tissue immersion optical clearing in terahertz biophotonics," *Journal of Biophotonics*, vol. 13, no. 12, p. e202000297, 2020.

[31] J. Kölbel *et al.*, "Terahertz dynamics in the glycerol-water system," *Phys. Rev. B*, vol. 107, p. 104203, Mar 2023. [Online]. Available: https://link.aps.org/doi/10.1103/PhysRevB.107.104203

[32] Y. Desmet, "Echantillonnage de signaux radar par voie optoélectronique : étude des non-linéarités des photoconducteurs à cavité résonante," Ph.D. dissertation, École doctorale Sciences pour l'ingénieur (Lille), 5 2018. [Online]. Available: https://www.theses.fr/2018LILUI019

[33] J. F. Roux *et al.*, "RF frequency response of photoconductive samplers," *IEEE Journal of Quantum Electronics*, vol. 47, no. 2, pp. 223–229, Feb. 2011.